Cell Reports
Physical Science

CellPress
OPEN ACCESS

Article

Characterization of multiterminal tandem photovoltaic devices and their subcell coupling

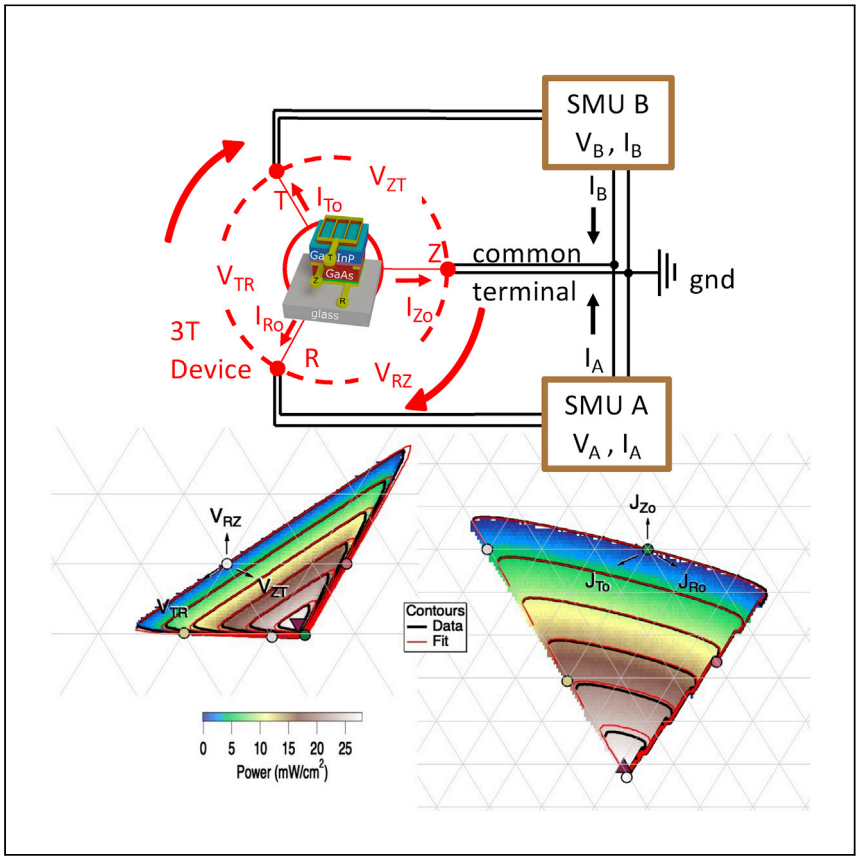

Three- and four-terminal tandem photovoltaic devices are becoming increasingly relevant. Geisz et al. demonstrate meaningful measurement techniques for unambiguously characterizing these devices using 3T GaInP/GaAs tandem solar cells as examples. Subcell coupling is sensitively quantified with coupled dark measurements that are fit to a simple equivalent optoelectronic circuit.

John F. Geisz, William E. McMahon, Jeronimo Buencuerpo, Michelle S. Young, Michael Rienäcker, Adele C. Tamboli, Emily L. Warren

john.geisz@nrel.gov

Highlights

Two types of 3T GaInP/GaAs tandems are fabricated and characterized

Hexagonal plots unambiguously characterize multiterminal tandem solar cells

Five zero-power points of 3T tandems are analogous to the V_{OC} and J_{SC} of 2T devices

Tiny luminescent coupling from the bottom to the top subcell of 3T tandem is quantified

Geisz et al., Cell Reports Physical Science 2, 100677
December 22, 2021
https://doi.org/10.1016/j.xcrp.2021.100677

Cell Reports
Physical Science

CellPress
OPEN ACCESS

Article

Characterization of multiterminal tandem photovoltaic devices and their subcell coupling

John F. Geisz,[1,3,*] William E. McMahon,[1] Jeronimo Buencuerpo,[1] Michelle S. Young,[1] Michael Rienäcker,[2] Adele C. Tamboli,[1] and Emily L. Warren[1]

SUMMARY

Three-terminal (3T) and four-terminal (4T) tandem photovoltaic (PV) devices using various materials have been increasingly reported in the literature, but measurement standards are lacking. Here, multiterminal devices measured as functions of two load variables are characterized unambiguously as functions of three device voltages or currents on hexagonal plots. We demonstrate these measurement techniques using two GaInP/GaAs tandem solar cells, with a middle contact between the two subcells, as example 3T devices with both series-connected and reverse-connected subcells. Coupling mechanisms between the subcells are quantified within the context of a simple equivalent optoelectronic circuit. Electrical and optical coupling mechanisms are most clearly revealed using coupled dark measurements. These measurements are sensitive enough to observe very small luminescent coupling from the bottom subcell to the top subcell in the prototype 3T device. Quick simplified measurement techniques are also discussed within the context of the complete characterization.

INTRODUCTION

Inexpensive silicon solar cells are an amazing success story that has revolutionized energy production on Earth in recent years, but efficiencies are nearing practical limits and energy demand eventually will be limited by area constraints. Therefore, demand for higher-efficiency solar cells will continue to increase and multijunction solar cells will be required. Building upon groundwork laid by III-V multijunction solar cells that have been studied, perfected, and used in area-constrained applications such as space and concentrating photovoltaics, a host of new multijunction solar cell material systems have been proposed for one-sun applications.

Most single- and multijunction solar cells currently use two electrical terminals (2T), but three-terminal (3T) and four-terminal (4T) devices have been actively investigated. All-III-V 3T tandem devices grown by a single epitaxial process have been demonstrated with lateral conductive layers for middle contacts.[1–5] Mechanically stacked III-V on silicon tandems have been demonstrated in 4T[6–9] and 3T[10–13] configurations. Perovskite on silicon 3T tandems are particularly interesting for their low-cost potential.[14–17] Interdigitated back contact (IBC) cells have considerably simplified the fabrication of 3T tandems on silicon,[18–20] and single-junction IBC silicon solar cells can be 3T devices in their own right.[21]

Although 2T tandems are simple to use, 3T and 4T multiterminal devices have some significant advantages. Multiterminal device designs can circumvent restrictions on

[1]National Renewable Energy Laboratory (NREL), Golden, CO 80401, USA

[2]Institute for Solar Energy Research Hamelin (ISFH), 31860 Emmerthal, Germany

[3]Lead contact

*Correspondence: john.geisz@nrel.gov

https://doi.org/10.1016/j.xcrp.2021.100677

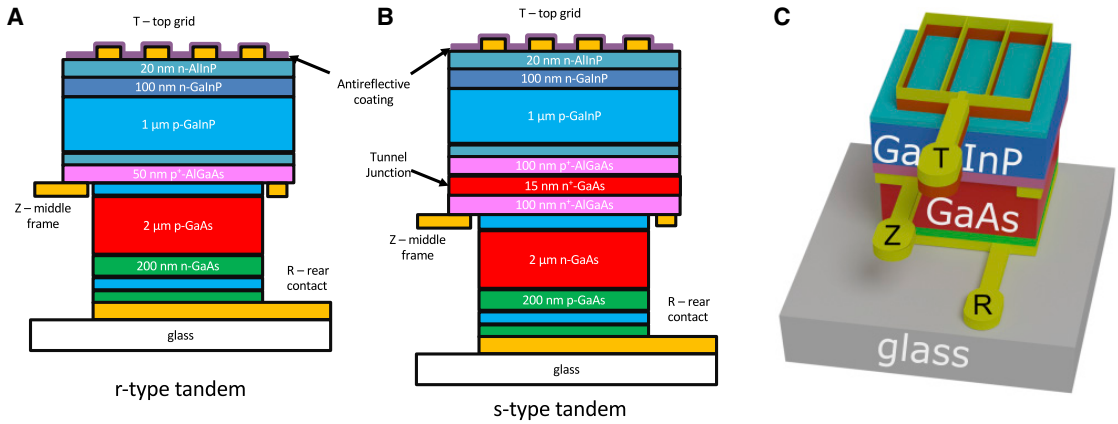

Figure 1. Schematics of GaInP/GaAs 3T device structures

(A) Layer structure of an r-type GaInP/r/GaAs 3T tandem.

(B) Layer structure of an s-type GaInP/s/GaAs 3T tandem with a tunnel junction interconnection.

(C) Three-dimensional schematic showing external top (T), middle (Z), and rear (R) contacts.

series-connected 2T multijunction solar cells such as requirements for polarity-changing interconnections (e.g., tunnel junctions) and current-matched designs (e.g., band gaps and absorber thicknesses defined by the spectrum). 3T and 4T devices can also improve energy yields over 2T multijunction devices in cases of changing terrestrial spectra.[22] However, these advantages result in complications in stringing individual cells into modules. Voltage-matched (VM) approaches have been proposed[23,24] to address these complications and have recently been demonstrated.[25,26] Warren et al.[27] proposed a taxonomy for naming contacts in 3T photovoltaic (PV) devices to help standardize nomenclature, but standards for multiterminal characterization have not yet been reported. Meaningful 3T and 4T measurements are required to determine the peak cell efficiency, characterize the expected performance within various string configurations, and quantify the important coupling mechanisms by fitting to simple models.

In this paper, we propose fundamental techniques and principles for measurement and characterization of 3T photovoltaic devices that can also be applied to 4T tandem devices. We demonstrate them using measurements of prototype GaInP/GaAs 3T devices. Many types and polarities of 3T devices are possible,[27] but we demonstrate these techniques here using an all-III-V device with back-to-back diodes that has been named r-type (for reverse connected) and an all-III-V device with diodes pointing in the same direction called s-type (for series connected). The data for the s-type device is presented in the supplemental information. III-V 3T tandems are ideal for this initial demonstration of these techniques, because III-V multijunction solar cells have been studied, perfected,[28] and used for area-constrained applications such as space and concentrating photovoltaics and are therefore highly stable, configurable, and well understood. III-V tandem solar cells also show strong luminescent coupling and are thus ideal for studying this coupling mechanism in 3T devices.

RESULTS AND DISCUSSION

Fabrication

Inverted two-junction GaInP/GaAs solar cells (Figure 1) are grown lattice matched onto single-crystal GaAs substrates by atmospheric-pressure organometallic vapor-phase epitaxy (OMVPE). The thin tandem device is processed from the back

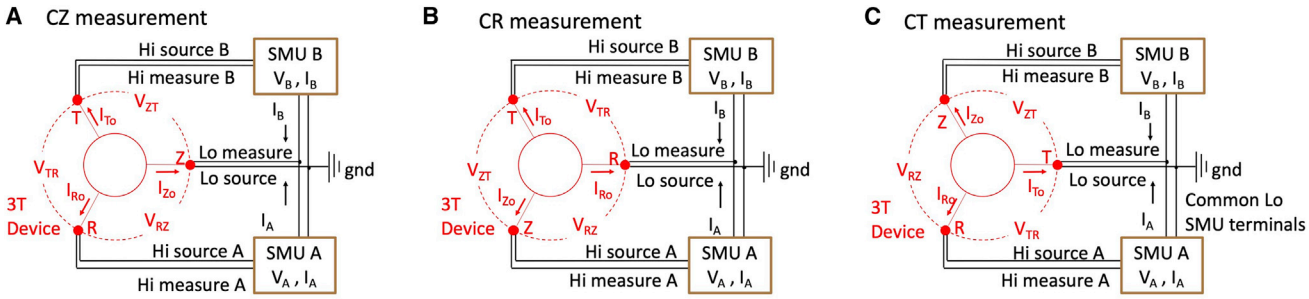

Figure 2. Three possible measurement configurations for the same 3T device

(A) CZ mode.

(B) CR mode.

(C) CT mode.

The 3T devices are shown in red. The measurement equipment shown in black is the same in all cases, with the low terminals of two source meter units (SMUs) held in common. The "o" denotes current flowing out of a contact.

side, attached to glass with clear epoxy, removed from the GaAs substrate, and processed from the front side.[29] This fabrication provides externally accessible top, middle, and bottom metal contacts, as shown in Figure 1C. The processing is similar to the inverted metamorphic multijunction (IMM) device,[30] but the structure is lattice matched. In this article, we characterize a GaInP(np)/r/GaAs(pn) tandem without a tunnel junction, as shown schematically in Figure 1A. The middle contact is an open metal frame around the perimeter of a 5 × 5 mm device contacting a 50-nm-thick $Al_{0.3}Ga_{0.7}As$:C p-type layer between the subcells. The lateral electrical transport to the surrounding middle contact takes place primarily within the p-type absorber layers of the two subcells (and the connecting p+-AlGaAs layer). The top subcell contains a 1-μm-thick p-type GaInP absorber layer, and the bottom subcell contains a 2-μm-thick p-type GaAs absorber layer. Both of these layers contribute to the lateral conductance of the middle (Z) contact. A transmission line measurement (TLM) indicates that the sheet resistance of the p-type GaInP layer alone is about 272 ohms/square, providing an upper bound, but the sheet resistance of the p-GaAs layer could not be measured within the TLM structure because it is etched away during processing. An antireflective coating of 100 nm of MgF_2 and 50 nm of ZnS was deposited by thermal evaporation as a final step. In the supplemental information, data for a similarly processed GaInP(np)/s/GaAs(np) 3T tandem with a tunnel junction, shown in Figure 1B, are also presented. This s-type structure also works well as a 2T device when the Z contact is not used and is similar in structure to very-high-efficiency GaInP/GaAs tandems that have reached 32.8% efficiency.[31]

Measurement setup

Schematics of 3T measurements are shown in Figure 2. A generic 3T device is represented by the red portions in Figure 2 using the taxonomy of Warren et al.[27] Every 3T PV device has a well-defined top (T), rear (R), and extra (Z) electrical contact, as labeled in Figure 1 for the specific GaInP/GaAs devices used in this work. The 3T devices were measured here with two Keithley 238 source-meter units (SMUs), as shown in black in Figure 2, but a dual-channel SMU[13] could also be used. The 3T device was connected to the two SMUs in common Z (CZ), common R (CR), or common T (CT) modes, as shown in Figures 2A–2C, respectively. Either both voltages (V_A, V_B) or both currents (I_A, I_B) were systematically scanned as independent variables from the software. Each measurement pair (e.g., I_A, I_B) corresponding to the scanned source pair (e.g., V_A, V_B) was collected by the computer before moving to the next measurement. For each measurement, the current (I) or voltage (V) of each SMU

was set, a single software trigger was sent to one SMU, and the other SMU was simultaneously initiated with an external electrical trigger connection. In addition, appropriate compliance values were set to prevent the 3T device from being damaged by driving beyond breakdown. Whenever compliance was detected on either SMU, the measurement values of both SMUs were discarded and replaced with not-a-numbers (NaNs) to eliminate non-sensical results. Full 2D maps could take from 10 minutes to 1 hour depending on data range, resolution, and communication speeds. Typically, about 2 data points per second were collected. Theoretically, the measurement speed could be increased by scanning through several measurements (at least in one dimension) controlled entirely by the SMU, but care must be taken to prevent transient effects as the measurement is sped up. This may become an important consideration for materials such as perovskites that experience significant measurement hysteresis.[32] We included a minimum 10 ms delay before each measurement point for these III-V devices. Most measurements were scanned from forward to reverse bias, but no differences were observed when measured from reverse to forward, as is typical for standard III-V solar cells as used here.

The optical illumination, which may be a standard reference spectrum (e.g., AM1.5G), can be challenging to produce for multijunction devices and is usually simulated in the laboratory to collect the appropriate number of photons in each junction,[33] rather than creating the true spectral shape. Before the current-voltage (I-V) measurements described earlier were taken, the simulator illumination intensity was set and characterized with matched reference isotype cells. Spectral mismatch correction was performed based on measured spectral irradiance of the simulator and external quantum efficiency (EQE) of the actual 3T device shown in Figure S9, as is typical for multijunction measurements.[33] White Xe light from a Spectrolab XT-10 solar simulator was supplemented with a blue 470 nm collimated high-power light emitting diode to achieve one-sun AM1.5G illumination on each subcell. More details on setting the illumination can be found in the supplemental experimental procedures. The EQE of each junction of a 3T tandem (i.e., RZ or TZ) was measured in the CZ mode separately while holding the other junction (i.e., TZ or RZ) shorted. Shorting the other junction prevents the possibility of significant luminescent coupling artifacts[34] by draining the recombination current that could drive light emission. In this measurement configuration, no light or voltage bias was required. For s-type 3T tandems, the EQE could also be measured and corrected for luminescent coupling by light biasing and measuring the junctions in series (i.e., TR), as for 2T devices.[35]

Three-terminal device variables

Two-terminal PV devices under a well-defined illumination spectrum (or in the dark) can be fully characterized by measuring I as a function of V or by measuring V as a function of I. In other words, an I-V curve with one independent variable and one dependent variable defines its electrical performance characteristics for any given optical illumination. This characterization has been well established and can be further used to fit to simplified physical models of the device.

Three-terminal devices are considerably more complicated to characterize than 2T devices. For every well-defined illumination spectrum $\Phi(\lambda)$, 6 variables define a unique electrical state of the device [I_{Ro}, I_{Zo}, I_{To}, V_{ZT}, V_{RZ}, V_{TR}], where o indicates the current is flowing out of the cell. These electrical parameters are not independent. Kirchoff's laws require the following:

$$I_{Ro} + I_{Zo} + I_{To} = 0 \quad \text{(Equation 1)}$$

and

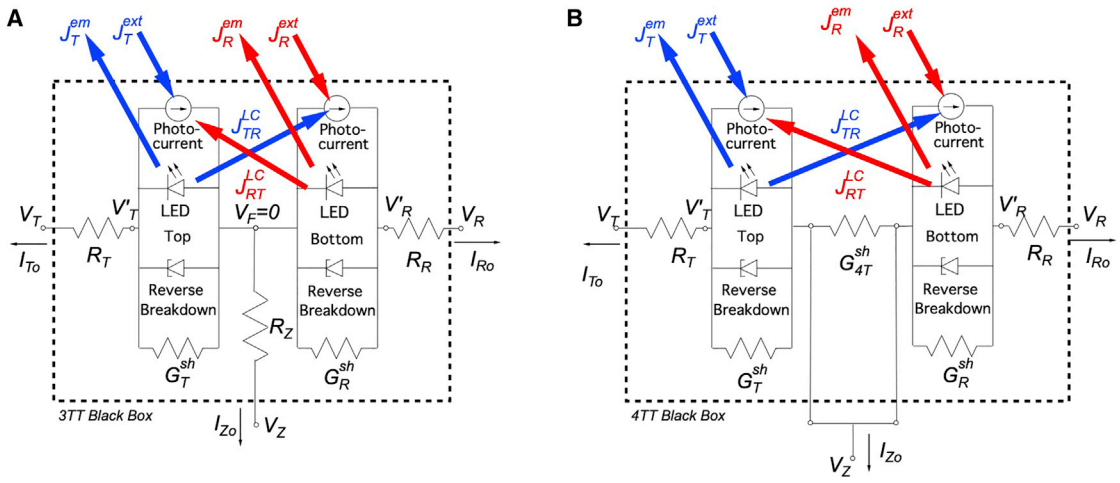

Figure 3. Equivalent optoelectronic circuit of two-junction tandem devices

(A) 3T tandem device.

(B) 4T tandem device measured as a 3T tandem.

Coupling between the subcells occurs through luminescent coupling (J_{TR}^{LC} and J_{RT}^{LC}) and shared resistance R_Z. The external illumination J^{ext} and the emitted light J^{em} of the top and rear subcells is also indicated on the figure. The direction of the top and bottom diodes can be reversed for devices with different polarities. The numerical solution of the 3T model is described in the supplemental experimental procedures.

$$V_{ZT} + V_{RZ} + V_{TR} = 0 \qquad \text{(Equation 2)}$$

The specific diode operating characteristics of the two coupled subcells within the 3T device will determine two more of these parameters. Thus, a unique electrical operating state can be obtained by simultaneously setting two of the 6 variables (one from each subcell), measuring two more, and calculating the rest from Equations 1 and 2.

Coupling mechanisms

Tandem solar cells can be highly coupled both optically and electrically, as shown in the equivalent optoelectronic circuit diagrams in Figure 3. Optical coupling through luminescence has been studied for 2T tandems,[34–37] 3T tandems,[38] and 4T tandems[39,40] and occurs significantly whenever one subcell is driven toward forward bias to emit light and another subcell can absorb some emitted light. The luminescent coupling current density J_{ij}^{LC} generated in one subcell j is proportional[41] to the density of electroluminescent photons J_i^{em} that are emitted from the front of the device by the other subcell i as a result of reciprocity:[42]

$$J_{ij}^{LC} = \beta_{ij}\, J_i^{em} = \beta_{ij}\, J_i^{db}\left[e^{\frac{qV_i'}{kT}} - 1\right] \qquad \text{(Equation 3)}$$

where $J_i^{db}(\tilde{E}_i^g, T)$ is the reverse saturation current in the detailed balance limit[41,43] given in Equations S3 and S4 and $V\prime_i$ is the voltage across subcell i without series resistance. The proportionality constant β_{ij} is related to the emission wavelength, absorption spectra, and optical geometry[40,44] and can be as high as $4n^2$ for J_{TR}^{LC}, where n is the index of refraction. J_{RT}^{LC} is typically negligibly small. In 4T tandems, the subcells and their optical coupling can be characterized by connecting the two subcells externally, as shown in Figure 3B, and measuring them as a 3T tandem.[45] However, measuring a 4T tandem in this way does not characterize shunting in the electrical insulation between the subcells. (This shunting is indicated by G_{4T}^{sh} in Figure 3B and should be characterized separately, because this may become important

in strings of 4T cells, where the top and bottom cell may be operating at significantly different voltages.)

Electrical coupling in 3T tandems occurs as a result of shared internal resistances[16,46] for direct current (DC) measurements. (Capacitive coupling may also be important in alternating current [AC] measurements, but we do not consider this here.) For example, driving large currents from the bottom subcell I_{Ro} through a common resistive Z contact (shown as R_Z in Figure 3A) will affect the voltage $V_{TZ} = (V_T - V_Z)$ because of the resistive drop through the Z contact. Thus, the current through one subcell affects the voltage across the other subcell. Because 4T tandems (Figure 3B) do not have a common internal resistance (i.e., $R_Z = 0$), electrical coupling is not expected. The behavior of R_Z in 3T tandems as a function of operating conditions becomes complicated as a result of distributed resistance[47] or bipolar IBC bottom cells,[48] but the model is still useful for understanding measurement considerations.

As a result of these coupling mechanisms, every 3T and 4T device measurement must control and specify the state of two independent variables, as described earlier. A simple I-V curve for a 3T or 4T device is ill defined unless another variable is constrained and reported with the measurement. As will be shown next, a two-dimensional image is required to capture the full behavior of the multiterminal device.

Relationship between device variables and load measurements

Because they are over-specified, not all 6 device variables described can be independently controlled. Instead, two load variables are sourced and two load variables are measured within the externally connected SMUs, and device variables must be determined from the load variables. Because of the convenient relationships 1 and 2, any 3T PV device can be characterized with only two loads, such as SMU A and B shown in Figures 2A–2C when measuring in CZ, CR, or CT modes, respectively. In this paper, we restrict the discussion to SMUs connected together at the low side, as shown in Figure 2, but other equipment configurations are possible. (Further complications in experimental setup can result by swapping which SMU is connected to which non-common terminal and which SMU terminal is common to the other SMU.) We use separate current and voltage probes to reduce the effects of resistances in the circuit external to the 3T device as much as possible. We also electrically ground the source side of these common-low terminals to prevent the possibility of developing large voltages relative to ground. Thus, we can measure and characterize a 3T device by simultaneously measuring two load variables as functions of the other two sourced load variables:

$$\begin{cases} I_A^{mode}\left(V_A^{mode}, V_B^{mode}\right) \\ I_B^{mode}\left(V_A^{mode}, V_B^{mode}\right) \end{cases} \quad \text{(Equation 4)}$$

and/or

$$\begin{cases} V_A^{mode}\left(I_A^{mode}, I_B^{mode}\right) \\ V_B^{mode}\left(I_A^{mode}, I_B^{mode}\right) \end{cases} \quad \text{(Equation 5)}$$

Here, "mode" indicates the equipment measurement mode, CZ, CR, or CT (i.e., how the loads were connected to the device, as shown in Figure 2), and the measurement mode must be specified to unambiguously indicate the load variables of SMU A and B. Because we have two dependent variables as functions of two independent variables, this results in two 2D images of either currents (Equation 4) or voltages

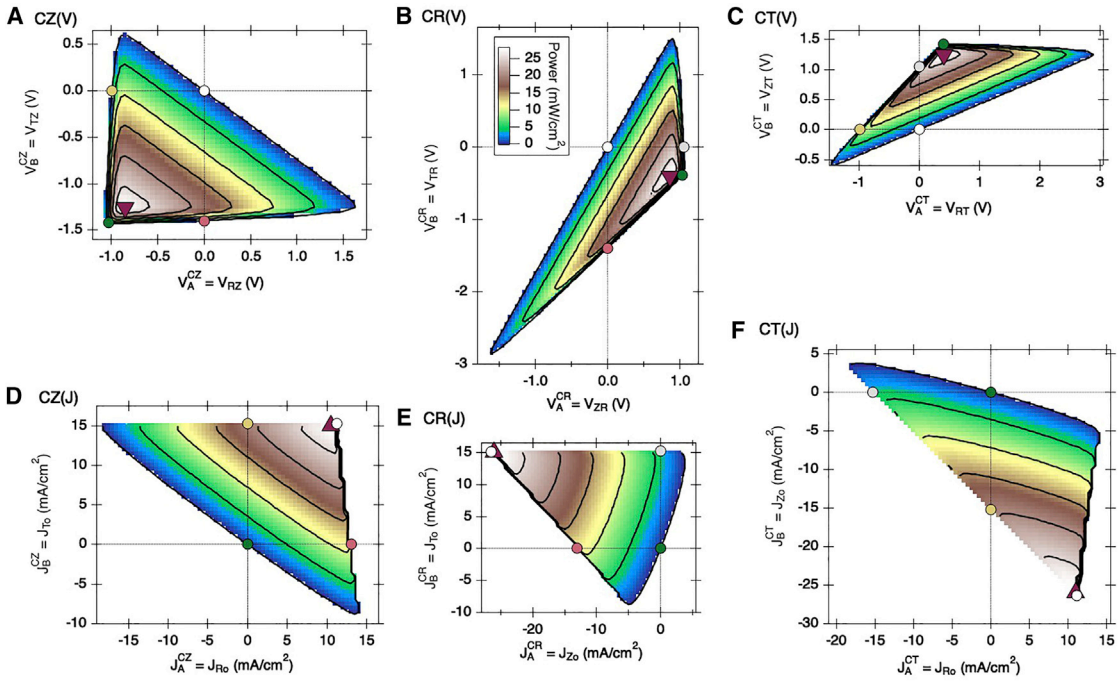

Figure 4. Load-plane plots of six separate 2D measurements of a 3T GaInP/r/GaAs device (MS874) at one-sun AM1.5G illumination

(A and D) Measured in the CZ measurement mode.

(B and E) Measured in the CR measurement mode.

(C and F) Measured in the CT measurement mode.

Power density (in milliwatts per square centimeter) indicated by the color as quantified in the inset of (B) is plotted as a function of load voltages (A–C, every 0.05 V) and load current densities (D–F, every 0.5 mA/cm^2). Black iso-power contours are also shown every 5 mW/cm^2 from 0 to 25. Special points are shown as colored markers on all plots, as tabulated in Figure 7. The red triangles indicate the MPP of each dataset, and the colored circle markers show the easily measured zero-power points for each dataset, which correspond to the colors in Figure 7.

(Equation 5). Typically, these equipment-dependent, multidimensional results are reported parametrically as power density,

$$P_{tot} = -\left(I_A^{mode} \cdot V_A^{mode} + I_B^{mode} \cdot V_B^{mode}\right) \Big/ A_{3T}$$

$$= -J_A^{mode} \cdot V_A^{mode} - J_B^{mode} \cdot V_B^{mode}, \qquad \text{(Equation 6)}$$

for every measurement mode shown in Figure 2. The negative sign is applied so that positive P_{tot} indicates that the solar cell is producing power and the loads are consuming power. The plots of $P_{tot}(V_A^{mode}, V_B^{mode})$ or $P_{tot}(J_A^{mode}, J_B^{mode})$, often denoted as P-V-V or P-J-J, are plotted as functions of the load coordinates sourced by the SMUs. These plots are shown in Figure 4 for the prototype GaInP/r/GaAs 3T device for each of the measurement modes described in Figure 2. Similar measurements of the GaInP/s/GaAs device are shown in Figure S5. Here, A_{3T} is the full (or largest) area of the 3T device, and we define the individual current densities relative to that full area:

$$J_A^{mode} \equiv I_A^{mode} \Big/ A_{3T}$$
$$J_B^{mode} \equiv I_B^{mode} \Big/ A_{3T} \qquad \text{(Equation 7)}$$

Using this convention, P_{tot} (in milliwatts per square centimeter) is equal to the efficiency (as a percentage) when illuminated with a one-sun irradiance of 100 mW/cm^2. Both subcells may not have the same area, as shown schematically in Figure 1A

for the III-V prototype cell used here. In this case, the area of the bottom subcell is only 89% that of the top subcell because of the area required for the intermediate middle contact. Therefore, when interpreting the results, the photocurrent density (as defined earlier) generated in the bottom subcell must be understood to be scaled by A_{bot}/A_{3T} relative to the actual photocurrent density that may be calculated, for example, by the integrated EQE.

Although 3T data have been reported most often only as functions of independently varied voltages,[12,13] important information can be observed in the P-J-J load-plane plots[27] that is hidden in the P-V-V load-plane plots. For example, luminescent coupling can be directly observed in the P-J-J data as a slope of the zero-power contour (i.e., the right side of Figures 4D and 4F, but see also the differences in fitting in Figure 6). This is not apparent in the P-V-V data. It is therefore quite useful to measure both P-V-V and P-J-J data, because equally spaced data in one parameter space can become quite sparse when plotted as functions of the other variables.

Previously in the literature,[5,12,13,45] measurements of 3T devices have been reported as functions of load two variables, but depending on how a 3T device is connected to the loads (see Figure 2), seemingly different results are obtained, as shown in Figure 4. This can sometimes become a source of confusion around 3T measurements, because the measurement configuration is not always well specified. In our paper,[45] a 4T GaInP//Si device was connected as an s-type 3T tandem (see Figure 3B), measured in the CR mode (this was called the 3T configuration in Figure 2d of Schnabel et al.[45]) and compared with the same 4T device measured in the CZ mode (called the 4T configuration in Figure 2a of Schnabel et al.[45]). Tayagaki et al.[13] were careful to measure and specify their 3T tandem device as a function of load voltages in CZ, CR, and CT modes. These papers concluded that the peak efficiency is the same, no matter which measurement mode was used. We can further say that every operating point in a particular mode corresponds to an equivalent device state within each of the other measurement modes. To report unambiguous results that are not equipment dependent, it is best to report simultaneous I-V curves in the form of the device parameters

$$\begin{cases} I_{Ro}(V_{ZT}, V_{RZ}, V_{TR}) \\ I_{Zo}(V_{ZT}, V_{RZ}, V_{TR}) \\ I_{To}(V_{ZT}, V_{RZ}, V_{TR}) \end{cases} \quad \text{(Equation 8)}$$

and/or

$$\begin{cases} V_{ZT}(I_{Ro}, I_{Zo}, I_{To}) \\ V_{RZ}(I_{Ro}, I_{Zo}, I_{To}), \\ V_{TR}(I_{Ro}, I_{Zo}, I_{To}) \end{cases} \quad \text{(Equation 9)}$$

where, for example, $V_{ZT} = V_Z - V_T$ and I_{Ro} indicate the current out of the device, as shown in Figure 2. Again, because these results cannot be represented in a single graph, we plot them parametrically as functions of the power density from Equation 6:

$$P_{tot}(V_{ZT}, V_{RZ}, V_{TR}) \quad \text{(Equation 10)}$$

and/or

$$P_{tot}(I_{Ro}, I_{Zo}, I_{To}) \quad \text{(Equation 11)}$$

All of these device parameters [I_{Ro}, I_{Zo}, I_{To}, V_{ZT}, V_{RZ}, V_{TR}] can be calculated from the load parameters [I_A, I_B, V_A, V_B] based on a rather simple analysis of the electrical circuits shown in Figure 2, but the analysis is different for every possible equipment

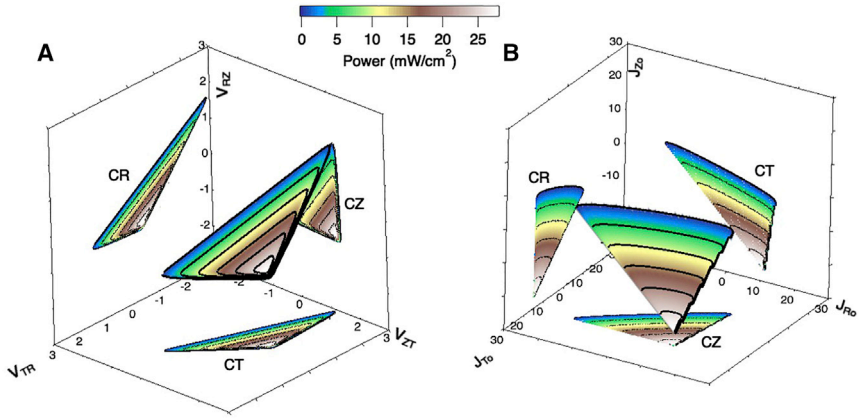

Figure 5. 3T GaInP/r/GaAs device measurements from Figure 4 replotted as functions of 3D device coordinates

(A) $P_{tot}(V_{ZT}, V_{RZ}, V_{TR})$, where voltages have units of volts.

(B) $P_{tot}(J_{Ro}, J_{Zo}, J_{To})$, where current densities have units of milliamperes per square centimeter.

The power density is indicated by the color bar, with black iso-power contours every 5 mW/cm^2. Each raw dataset from Figure 4 is plotted on its plane of origin (CZ, CR, or CT). The CZ measurements are projected onto the 3D device plane using Equations 1 and 2. Rotation of these 3D plots in video format can be observed in Videos S1 and S2.

configuration. We find it convenient to calculate the equipment-independent device parameters from the measured load parameters using equipment-dependent matrices. Such conversion matrices can be written for every different equipment configuration, such as CZ, CR, and CT shown in Figures S1–S3, respectively, as given in Equations S13–S24, or any other equipment configuration that one can imagine.

The P-V-V-V and P-J-J-J plots are displayed as functions of 3 dimensions, as shown in Figures 5A and 5B, respectively (as calculated from the CZ mode data). Although these 3D plots can be difficult to fully visualize on a printed page, we can rotate them to understand them (see Videos S1 and S2). We immediately see from Figure 5 that these 3D data fall onto 2D plane surfaces. This is a consequence of Kirchhoff's laws in Equations 1 and 2, and we denote it as the device coordinate plane. The projections of the 3D device data onto the load planes (e.g., V_{RZ}-V_{TR} plane for CR) result in the original 2D load data for each measurement mode. By viewing the device coordinate plane in 3D from the isometric viewpoint, we see that this 3D data can be flattened to a 2D hexagonal device-plane plot, as shown in Figure 6. The isometric transformation of the 3D data into Cartesian coordinates for hexagonal plots is given in Equations S11 and S12. To be able to understand and quantify the hexagonal plot, regular lines of constant J_{Ro}, J_{Zo}, J_{To}, V_{ZT}, V_{RZ}, or V_{TR} are plotted to form a hexagonal grid. The hexagonal plots for data measured in CR and CT modes are nearly identical to the transformed CZ data within the measurement uncertainty, as shown in Figure S4, demonstrating that the operating characteristics of the 3T device do not depend on the measurement configuration. These hexagonal plots are convenient 2D representations of the device characteristics that can be printed onto a page yet show the multidimensional nature of the device operation. The hexagonal plots of the GaInP/s/GaAs device shown in Figure S7 and fit in red using the parameters in Table S2 correspond to the load measurements in Figure S5.

Measurement simplifications

Although the complete unambiguous characterization of 3T devices with hexagonal P-V-V-V and/or P-J-J-J device-plane plots is comprehensive and ideal, these

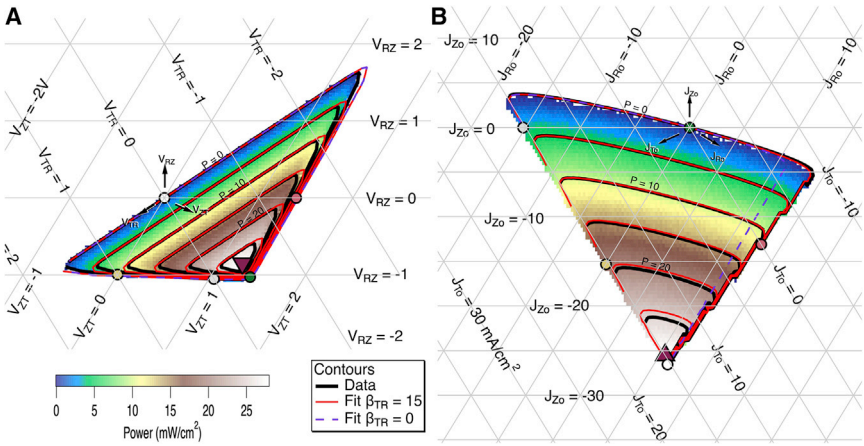

Figure 6. Hexagonal device-plane plots for the 3T GaInP/r/GaAs device

(A) $P_{tot}(V_{ZT}, V_{RZ}, V_{TR})$, with units of volts.

(B) $P_{tot}(J_{Ro}, J_{Zo}, J_{To})$, with units of milliamperes per square centimeter.

Measurements were taken at one-sun AM1.5G illumination in the CZ measurement mode, converted to device coordinates using Equations S13 and S14, and flattened to 2D using Equations S11 and S12. Data measured in CR and CT modes and transformed in this way appear nearly identical, as shown in Figure S4. The power density of the data is indicated by the color bar, with black iso-power contours every 5 mW/cm^2. Red iso-power contours show the results of fitting the model shown in Figure 3A with parameters listed in Table S1. The dashed purple zero-power contour shows the fit if the luminescent coupling parameter β_{TR} is changed to zero. Special zero-power points are shown as colored circle markers, as tabulated in Figure 7. The triangle markers indicate the MPP.

measurements may take considerable time. In some cases, it may be enough to characterize a subset of these values for substantial time savings, which can be particularly useful for metastable devices. These simple parameters are analogous to characterizing the short-circuit current density (J_{SC}), open-circuit voltage (V_{OC}), and maximum power point (MPP) in a 2T measurement. The following special points can be extracted from the measured 2D data of 3T devices with numerical techniques but can also be directly measured quickly with greater resolution than the 2D data, because the independent variables are constrained to only one or zero dimensions.

Zero-power contour

Just as J_{SC} and V_{OC} are important, interesting, and characteristic zero-power-producing points on a typical 1D current density versus voltage (J-V) curve, so is the entire zero-power contour of a 2D power plot of 3T devices. Although it is not generally easy to trace the entire zero-power (P = 0) contour of a 3T device without also measuring many other points on the 2D plot, we can identify five special points on the zero-power contour, by examining Equation 6, that are easy to measure because they can be defined by either load or device variables. The conditions for these points, listed in Table 1, result in zero-power points for every measurement mode, but when measured in different modes, the 3rd, 4th, and 5th conditions, as defined in load coordinates, correspond to differently numbered conditions in device coordinates. The first four special points in load variables can be quickly and easily measured by directly setting two of the load variables to zero. Although the fifth condition in load variables is not as easy to measure, it could be experimentally determined by a single 1D constrained line measurement. This is shown as a gray line in Figure 8B by setting $J_B^{CZ} = -J_A^{CZ}$ and finding where it simultaneously crosses $V_B^{CZ} = V_A^{CZ}$ in Figure 8C. It identifies the 3rd point listed under the device coordinates (gray

Table 1. Special zero-power points of 3T measurements

	Device coordinates		Load coordinates	
1	$V_{TR} = V_{ZT} = V_{RZ} = 0$		$V_A^{mode} = 0$	$V_B^{mode} = 0$
2	$I_{To} = I_{Ro} = I_{Zo} = 0$		$I_A^{mode} = 0$	$I_B^{mode} = 0$
3	$I_{Zo} = 0$	$V_{TR} = 0$	$I_A^{mode} = 0$	$V_B^{mode} = 0$
4	$I_{To} = 0$	$V_{RZ} = 0$	$V_A^{mode} = 0$	$I_B^{mode} = 0$
5	$I_{Ro} = 0$	$V_{ZT} = 0$	$I_A^{mode} = -I_B^{mode}$	$V_A^{mode} = V_B^{mode}$

The conditions are defined as functions of device or load coordinates. Conditions 3–5 in device coordinates do not necessarily correspond the same conditions in load coordinates.

circular marker $I_{Zo} = 0$ and $V_{TR} = 0$). These special points can help bound the area of parameter space that is interesting for subsequent 2D measurements and may be useful for intuitive parameterization of a device. They are shown for the GaInP/r/GaAs device as colored circle markers in Figures 4, 6, and 7 and summarized in Figure 7. The corresponding special points of the GaInP/s/GaAs device are shown in Figure S10. We discuss later how the differences between some of these points are directly related to optical and resistive coupling.

Maximum power point

The MPP of a 3T device is, by definition, the most desirable operating point for power extraction. It is always located somewhere within the island of the zero-power contour but is not generally simple to locate without 2D mapping. The MPP of our example GaInP/r/GaAs device has been determined from the maximum of each of the P-V-V and P-J-J datasets in each measurement mode and is reported in Figure 7 for points indicated by red triangles. The resulting MPP and its location in device coordinates are in good general agreement regardless of the measurement mode (in agreement with Tayagaki et al.[13]), but uncertainty arises from the wide data resolution required to minimize measurement times. (In this case, data were only measured every 0.05 V or 0.5 mA/cm^2.) This uncertainty because of resolution may be reduced through intelligent interpolation using an accurate model or polynomial fit, as is commonly done for simple 2T J-V curves.

When the coupling is relatively small, a simpler method of quickly estimating the MPP may be used. An iterative approach was used in Tayagaki et al.[49] by alternately measuring the top and bottom subcell J-V curves while holding the other subcell at its MPP from a previous measurement. Either the voltage or the current of one subcell is held constant while measuring the J-V curve of the other subcell in the CZ mode. The top subcell should always be measured first, because the magnitude of any luminescent coupling from bottom to top is always smaller than the luminescent coupling from top to bottom for different band-gap subcells. The best first measurement depends on the dominating coupling mechanism. If electrical coupling due to resistance is significant at MPP, it may be best to first measure the top subcell J-V while holding the bottom subcell at short circuit ($V_{RZ} = 0$), because the voltage drop across R_Z due to the current flow through the bottom subcell is similar to that at MPP. In the case of very large R_Z or injection-dependent R_Z (as with bipolar or low-doped unipolar IBC bottom subcells), it may instead be best to hold the bottom subcell at open circuit ($J_{Ro} = 0$) during the first measurement.[46] If luminescent coupling from the bottom to top subcell at MPP were strong, it would also be best to first measure the top subcell J-V while holding the bottom subcell at open circuit, but as mentioned earlier, this is usually not the case. After each iteration of J-V scans, a single simultaneous measurement of the two currents at the estimated MPP voltages is a good idea to confirm the

Color	Measurement Point	Mode	Measured Load Coordinates (mA/cm^2 or V) J_A	J_B	V_A	V_B	Calculated Device Coordinates (mA/cm^2 or V) J_{Ro}	J_{Zo}	J_{To}	V_{ZT}	V_{RZ}	V_{TR}	Total Power (mW/cm^2)
white	$V_{TR} = V_{ZT} = V_{RZ} = 0$	CZ	11.24	15.29	0.000	0.000	11.24	-26.54	15.29	0.000	0.000	0.000	0.00
		CR	-26.46	15.12	0.000	0.000	11.34	-26.46	15.12	0.000	0.000	0.000	0.00
		CT	11.16	-26.40	0.000	0.000	11.16	-26.40	15.24	0.000	0.000	0.000	0.00
green	$J_{To} = J_{Ro} = J_{zo} = 0$	CZ	0.00	0.00	-1.025	-1.421	0.00	0.00	0.00	1.421	-1.025	-0.396	0.00
		CR	0.00	0.00	1.025	-0.396	0.00	0.00	0.00	1.421	-1.025	-0.396	0.00
		CT	0.00	0.00	0.395	1.421	0.00	0.00	0.00	1.421	-1.025	-0.395	0.00
grey	J_{Zo}=0	CR	0.00	15.19	1.049	0.000	-15.19	0.00	15.19	1.049	-1.049	0.000	0.00
	V_{TR}=0	CT	-15.24	0.00	0.000	1.050	-15.24	0.00	15.24	1.050	-1.050	0.000	0.00
rose	J_{To}=0	CZ	13.09	0.00	0.000	-1.397	13.09	-13.09	0.00	1.397	0.000	-1.397	0.00
	V_{RZ}=0	CR	-13.04	0.00	0.000	-1.397	13.04	-13.04	0.00	1.397	0.000	-1.397	0.00
sand	J_{Ro}=0	CZ	0.00	15.32	-0.993	0.000	0.00	-15.32	15.32	0.000	-0.993	0.993	0.00
	V_{ZT}=0	CT	0.00	-15.22	-0.993	0.000	0.00	-15.22	15.22	0.000	-0.993	0.993	0.00
wine	Maximum	CZ	11.02	14.82	-0.850	-1.250	11.02	-25.84	14.82	1.250	-0.850	-0.400	27.89
	Power Point	CR	-25.81	14.80	0.850	-0.400	11.01	-25.81	14.80	1.250	-0.850	-0.400	27.86
	of P-V-V	CT	11.02	-25.81	0.400	1.250	11.02	-25.81	14.78	1.250	-0.850	-0.400	27.85
wine	Maximum	CZ	10.50	15.00	-0.887	-1.236	10.50	-25.50	15.00	1.236	-0.887	-0.349	27.85
	Power Point	CR	-26.00	15.00	0.850	-0.383	11.00	-26.00	15.00	1.233	-0.850	-0.383	27.84
	of P-J-J	CT	11.00	-26.00	0.383	1.235	11.00	-26.00	15.00	1.235	-0.852	-0.383	27.90
cyan	3 iteration	CZ 1st		14.78	0.000	-1.248							18.44
	quick	CZ 2nd	10.92	14.78	-0.863	-1.248							27.87
	MPP scans	CZ 3rd	10.92	14.80	-0.863	-1.248	10.92	-25.71	14.78	1.247	-0.863	-0.384	27.89
purple	MPP of 2:1 voltage constrained	CZ	11.23	14.68	-0.627	-1.254	11.23	-25.90	14.68	1.254	-0.627	-0.627	25.44
olive	MPP of 3:2 voltage constrained	CZ	11.11	14.75	-0.836	-1.254	11.11	-25.86	14.75	1.254	-0.836	-0.418	27.78

Figure 7. Values of special points of the GaInP/r/GaAs device in load coordinates and device coordinates

The shape and color of the markers correspond to those in Figures 4, 6, and 8.

MPP estimate. Regardless of which measurement is performed first, a good estimate of the tandem MPP may be quickly found if the value converges. Using this method, an estimate of the MPP of the example device was found for the GaInP/r/GaAs device and confirmed within three iterations, starting with the bottom subcell held at short circuit (shown as a light blue marker). Although plotted in Figure 8C, the first top-subcell J-V curve (black line) is difficult to differentiate from the third measurement (dashed blue line). The second (bottom subcell J-V) measurement, taken while holding the top subcell at V_{MPP} of the first measurement, is shown as a red line in Figures 8A and 8C.

Series-connected tandems

A 3T s-type tandem reduces to a 2T tandem device if the middle Z contact is not used. This constraint of J_{Zo} = 0 is easy to set with the CT and CR measurement modes. In the CZ measurement mode, this can be obtained by setting $J_B^{CZ} = -J_A^{CZ}$ while scanning over a range of current densities and measuring (V_A^{CZ}, V_B^{CZ}). This is an important comparison for s-type 3T tandems, because it can be used to justify the complicating efforts to create the third terminal and gives the J_{SC} of the corresponding 2T series-connected device (see supplemental information). For r-type 3T tandems, this constraint does not make sense for high efficiency (because the subcell voltages subtract, rather than add), but the measurement still provides value. This is the same condition as the gray line in Figure 8 that was described earlier to find the fifth zero-power point described earlier at which V_{TR} = 0 (or $V_B^{CZ} = V_A^{CZ}$). It also eliminates voltage loss or gain (in the case of the s-type 3T device shown in Figure S6) due to electrical coupling, because no current flows through the resistor R_Z shown in Figure 3A, and results in higher currents in the bottom subcell due to strong luminescence in the r-type device. This explains the improved fill factor of the gray line relative to the other J-V curves at MPP.

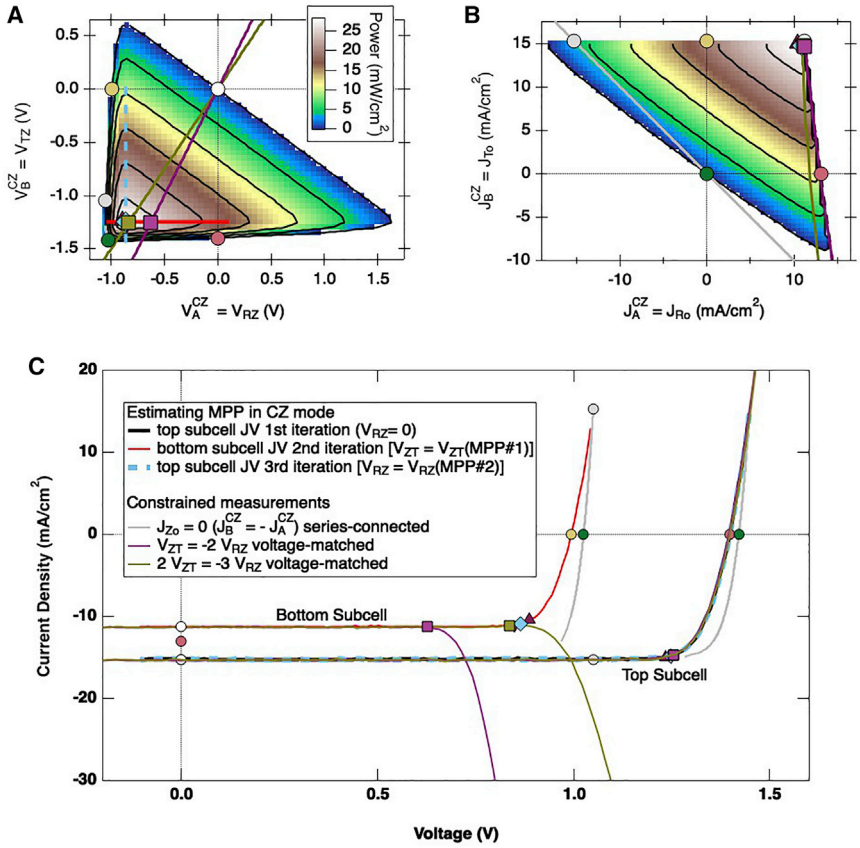

Figure 8. Simplified measurements of the 3T GaInP/r/GaAs device shown on top of full 2D data

(A) Power as a function of load voltages.

(B) Power as a function of load current densities.

(C) Current density as a function of the voltage for each subcell with signs chosen such that the 4th quadrant is the power-producing region. All measurements were performed in the CZ mode. The circular markers are the same zero-power points from Figures 4, 6, and 7. The triangle/square/diamond markers are MPPs under different measurement constraints, and the two markers of the same color in (C) are measured simultaneously, as tabulated in Figure 7. The red and cyan lines are the second and third measurements to iteratively find the MPP. They are constrained by the subcell V_{MPP} of the previous iteration J-V curve. The purple and olive lines are constrained to simulate operation within voltage-matched strings. The gray line is constrained to $J_{Zo} = 0$, which corresponds to the 2T series-connected operation (that produces little power for r-type tandems).

Voltage-constrained tandems

Various methods of stringing voltage-matched 3T tandems together have been proposed and demonstrated.[23–26] The CZ measurement mode of 3T tandems is most useful for voltage-matching constraints. In these stringing configurations, m series-connected bottom subcells are put in parallel with n top subcells, constraining the subcell voltages such that $V_B^{CZ}/\,V_A^{CZ} = \pm m/n$, where m and n are integers,[25] and the sign depends on whether the 3T tandem is s type or r type. When the voltage of one subcell is constrained by the voltage of the other subcell in an infinite string of 3T tandem devices, the performance of each 3T cell follows a 1D line that is a subset of the unconstrained 3T cell performance. Characterizing a single 3T tandem cell under voltage-constrained conditions is a good way to determine appropriate voltage ratios for stringing modules of 3T cells, although the end losses in finite-length strings are another important consideration.[25] In Figure 8A, we can see that the 3:2 voltage-constrained measurement (purple lines and

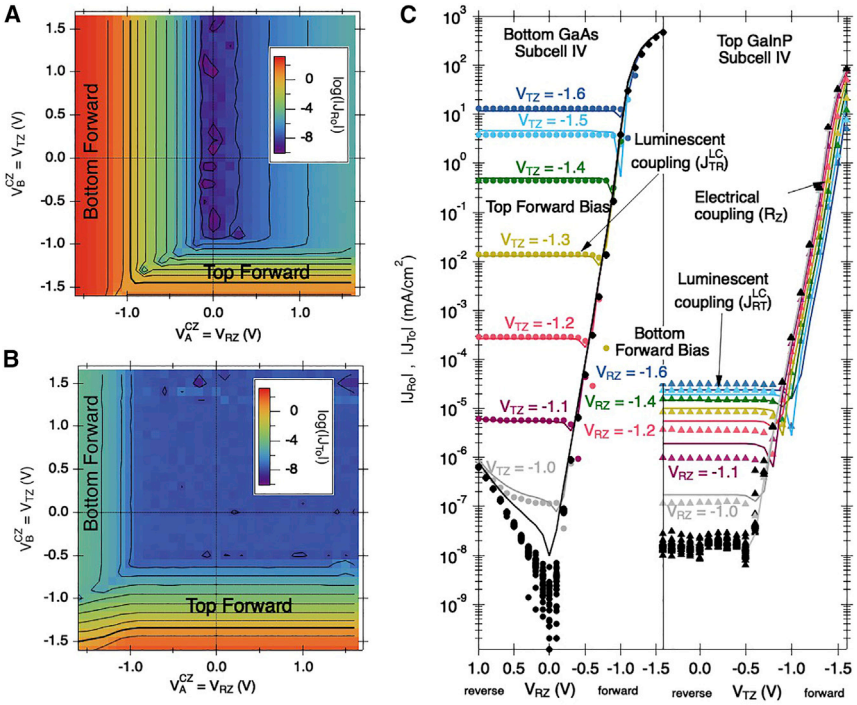

Figure 9. Coupled dark J-V measurements of GaInP/r/GaAs 3T device

Measurements were performed in the CZ mode as functions of $(V_A^{CZ}, V_B^{CZ}) = (V_{RZ}, V_{TZ})$ with 0.1 V spacing. The absolute value of the measured current densities (in milliamperes per square centimeter) are shown by color.

(A) $\log|J_{Ro}|$ for the bottom subcell.

(B) $\log|J_{To}|$ for the top subcell.

(C) Typical dark J-V plots of the bottom and top subcells are shown as functions of the voltage on the other subcell, with the voltages that lead to significant coupling highlighted by color. The measured data are shown as markers, and the lines show the fitting of the model shown in Figure 3A, with the parameters listed in Table S1. The voltages on the bottom axis are reversed so that forward bias is on the right. Coupling mechanisms in different regions are labeled.

marker) comes closer to the unconstrained MPP than the 2:1 voltage-constrained measurement (olive lines and marker). For this device, both the 2:1 and the 3:2 voltage-matching constraints exhibit strong luminescent coupling that increases the photocurrent of the bottom cell as the top cell is forced into large forward bias that results in significant light emission from the top subcell. This appears as though the bottom subcell current is heading in the wrong direction in Figure 8C. This behavior illustrates the extreme importance of recognizing the influence of coupling factors in 3T devices.

Coupled dark measurements

When superposition holds, dark current measurements can provide a powerful characterization tool. For single-junction and series-connected multijunction[41] 2T solar cells, we can sensitively fit various device models, such as the two-diode model with series and shunt resistance, to the dark J-V. Likewise, dark measurements of 3T PV devices are essential for sensitive fitting to models that include electrical and optical coupling mechanisms. We systematically measure the 3T dark currents in the CZ mode as functions of the two load voltages, as described in Equation 4. Because dark measurements of solar cells do not result in power production, power is not a good parametric function to use for plotting as with the light measurements.

Instead, we plot the more familiar dark J-V curves for both J_{To} versus V_{TZ} and J_{Ro} versus V_{RZ}. A family of curves with various voltage biases applied to the other subcell is shown in Figure 9 for our GaInP/r/GaAs 3T device and Figure S8 for the GaInP/s/GaAs device.

An important reason for characterizing any device is to understand and model the physics of the device. The optical and electrical coupling mechanisms become immediately apparent from this coupled dark measurement, primarily when at least one of the subcells is driven with high forward bias. The coupling can be understood in terms of the optoelectronic circuit shown in Figure 3A. The data in Figures 6 and 8 were fit with the numerical solution of this simple model described in the supplemental information, with parameters listed in Table S1. In the left panel of Figure 9C, the horizontal J-V curves show the photocurrent in the bottom subcell that results from luminescent coupling from the top subcell driven in forward bias (represented by J_{TR}^{LC} in Figure 3A). The model fit shown as lines using β_{TR} = 15.0 agrees well with the data shown as markers. In the right panel of Figure 9C, the horizontal curves show the photocurrent in the top subcell that results from luminescent coupling from the bottom subcell to the top subcell (represented by J_{RT}^{LC} in Figure 3A). The model shown as lines indicates that this is an extremely small amount of luminescent coupling from bottom to top that is typically neglected in 2T tandems unless the junctions have the same band gap[50] but is quantified here by $\beta_{RT} = 2 \times 10^{-6}$. This is the first time that this phenomenon has been directly observed for such a large difference in the subcell band gap. The reverse luminescent coupling is not observed in Figure S8 for the GaInP/s/GaAs device, possibly because the tunnel junction absorbs more of the emitted light. Finally, electrical coupling is illustrated on the far right side of the right panel of Figure 9C. Because the top and bottom subcells share a common Z terminal in this measurement, large bottom subcell forward-bias currents result in a voltage difference across R_Z that is added to the dark I-V curve of the top subcell.

These coupling mechanisms can also be understood through the zero-power points discussed previously and shown in Figure 8. The increased current density of the bottom subcell at V_{RZ} = 0 of the rose-colored circle marker (with J_{To} = 0) relative to the white circle marker (with V_{TZ} = 0) is explained by the luminescent coupling J_{TR}^{LC}. The increased bottom subcell voltage at J_{Ro} = 0 of the green circle marker (with $J_{To} = J_{Zo}$ = 0) relative to the sand-colored circle marker (with V_{TZ} = 0, but $J_{Zo} = -J_{To} = -15.2$ mA/cm^2) results from the voltage across the common resistance R_Z. The increased top subcell voltage at J_{To} = 0 of the green circle marker (with $J_{Ro} = J_{Zo}$ = 0) relative to the rose-colored circle marker (with V_{RZ} = 0, but $J_{Zo} = -J_{Ro} = -13.0$ mA/cm^2) also results from the voltage across the common resistance R_Z.

In conclusion, procedures and important considerations for three terminal tandem measurements are illustrated using robust and high-quality r-type (and s-type in the supplemental information) inverted GaInP/GaAs solar cells as examples. These procedures can also be applied to 4T tandem characterization. We show that 3T tandems can be characterized in several measurement modes using two loads. The measurement modes are equivalent and the measured characteristics can be transformed to unambiguous (mode independent) device characteristics of the 3T device. A two-dimensional hexagonal representation of light J-V measurements is proposed to simplify the presentation of the multidimensional device characterization. Simplifying measurements are also discussed to speed up characterization. In

particular, five easily measured zero-power-producing points analogous to the J_{SC} and V_{OC} of 2T measurements are identified that could provide intuitive insight into the subcell and coupling characteristics. Operationally constrained conditions relevant to cell operation within practical string configurations are also presented. Finally, coupled dark measurements of 3T tandems are discussed and linked to optical and electrical coupling mechanisms. Besides the typically observed luminescent coupling from the top cell to the bottom cell, we (for the first time) report sensitive observations consistent with small luminescent coupling from the low-band-gap bottom subcell to the high-band-gap top subcell. The measured data were well fit to a simple optoelectronic circuit model for 3T tandems that quantifies the effects of both optical and electrical coupling.

EXPERIMENTAL PROCEDURES

Resource availability

Lead contact

Further information and requests for resources should be directed to and will be fulfilled by the lead contact, John Geisz (john.geisz@nrel.gov).

Materials availability

This research did not generate unique materials.

Data and code availability

The authors declare that the data supporting the findings in the study are available within the article and the supplemental information. All other data and code are available from the lead contact upon reasonable request.

Materials and methods

See the supplemental experimental procedures for full details.

SUPPLEMENTAL INFORMATION

Supplemental information can be found online at https://doi.org/10.1016/j.xcrp.2021.100677.

ACKNOWLEDGMENTS

This work was supported in part by the United States (U.S.) Department of Energy (DOE) under contract DE-AC36-08GO28308 with Alliance for Sustainable Energy LLC, the manager and operator of the National Renewable Energy Laboratory, with funding provided by the Department of Energy Office of Energy Efficiency and Renewable Energy Solar Energy Technologies Office under contract SETP DE-EE00034911. The views expressed in the article do not necessarily represent the views of the DOE or the U.S. Government. For ISFH, the funding was provided by the German State of Lower Saxony and the German Federal Ministry for Economics and Energy (BMWi) within the research project 27Plus6 (FKZ03EE1056A). Thanks to Waldo Olavarria and Jeff Carapella for OMVPE growth at NREL.

AUTHOR CONTRIBUTIONS

Conceptualization and methodology: J.F.G. and W.E.M. Software, formal analysis, and writing – original draft: J.F.G. Investigation: J.F.G., J.B., and M.S.Y. Supervision, project administration, and funding acquisition: A.C.T. and E.L.W. Writing – review & editing: J.F.G., W.E.M., J.B., M.R., A.C.T., and E.L.W.

DECLARATION OF INTERESTS

The authors declare no competing interests.

Received: July 7, 2021
Revised: October 26, 2021
Accepted: November 15, 2021
Published: December 22, 2021

REFERENCES

1. Steiner, M.A., Wanlass, M.W., Carapella, J.J., Duda, A., Ward, J.S., Moriarty, T.E., and Emery, K.A. (2009). A Monolithic Three-Terminal GaInAsP/GaInAs Tandem Solar Cell. Prog. Photovolt. Res. Appl. *17*, 587–593. https://doi.org/10.1002/Pip.913.

2. Zehender, M., Antolin, E., Garcia-Linares, P., Artacho, I., Ramiro, I., Villa, J., and Marti, A. (2018). Module interconnection for the three-terminal heterojunction bipolar transistor solar cell. AIP Conf. Proc. *2012*, 040013. https://doi.org/10.1063/1.5053521.

3. Nagashima, T., Okumra, K., Murata, K., and Kimura, Y. (2000). Three-terminal tandem solar cells with a back-contact type bottom cell. In Proceedings of the 28th IEEE Photovoltaic Specialists Conference (IEEE), pp. 1193–1196. https://doi.org/10.1109/PVSC.2000.916102.

4. Wanlass, M.W., Ward, J.S., Emery, K.A., Gessert, T.A., Osterwald, C.R., and Coutts, T.J. (1991). High-performance concentrator tandem solar cells based on IR-sensitive bottom cells. Solar Cells *30*, 363–371. https://doi.org/10.1016/0379-6787(91)90069-2.

5. Zehender, M.H., Svatek, S.A., Steiner, M.A., García, I., Linares, P., and Warren, E.L. (2020). Inverted GaInP/GaAs Three-Terminal Heterojunction Bipolar Transistor Solar Cell. In Proceedings of the 47th IEEE Photovoltaic Specialists Conference (IEEE), pp. 1517–1521. https://doi.org/10.1109/PVSC45281.2020.9301000.

6. Gee, J.M., Loo, R.Y., Kamath, G.S., and R.C., K. (1985). A GaAs / Silicon mechanically stacked multijunction solar cell. In Proceedings of the IEEE Photovoltaic Specialists Conference (IEEE), pp. 546–551.

7. Partain, L.D., Fraas, L.M., McLeod, P.S., and Cape, J.A. (1985). High efficiency mechanical stack using a GaAsP cell on a transparent GaP wafer. In Proceedings of the IEEE Photovoltaic Specialist Conference (IEEE), pp. 539–545.

8. Essig, S., Allebé, C., Remo, T., Geisz, J.F., Steiner, M.A., Horowitz, K., Barraud, L., Ward, J.S., Schnabel, M., Descoeudres, A., et al. (2017). Raising the one-sun conversion efficiency of III–V/Si solar cells to 32.8% for two junctions and 35.9% for three junctions. Nat. Energy *2*, 17144. https://doi.org/10.1038/nenergy.2017.144.

9. VanSant, K.T., Simon, J., Geisz, J.F., Warren, E.L., Schulte, K.L., Ptak, A.J., Young, M.S., Rienäcker, M., Schulte-Huxel, H., Peibst, R., and Tamboli, A.C. (2019). Toward Low-Cost 4-Terminal GaAs//Si Tandem Solar Cells. ACS Appl. Energy Mater. *2*, 2375–2380. https://doi.org/10.1021/acsaem.9b00018.

10. Sakai, S., and Umeno, M. (1980). Theoretical analysis of new wavelength-division solar cells. J. Appl. Phys. *51*, 5018–5024. https://doi.org/10.1063/1.328382.

11. Schnabel, M., Rienäcker, M., Merkle, A., Klein, T.R., Jain, N., Essig, S., Schulte-Huxel, H., Warren, E., van Hest, M.F.A.M., Geisz, J., et al. (2017). III-V/Si Tandem Cells Utilizing Interdigitated Back Contact Si Cells and Varying Terminal Configurations. In Proceedings of the 44th IEEE Photovoltaic Specialist Conference (IEEE), pp. 3371–3375. https://doi.org/10.1109/PVSC.2017.8366003.

12. Schnabel, M., Schulte-Huxel, H., Rienäcker, M., Warren, E.L., Ndione, P.F., Nemeth, W., Klein, T.R., van Hest, M.F.A.M., Geisz, J.F., Peibst, R., et al. (2020). Three-terminal III–V/Si tandem solar cells enabled by a transparent conductive adhesive. Sustain. Energy Fuels *4*, 549–558. https://doi.org/10.1039/c9se00893d.

13. Tayagaki, T., Makita, K., Tachibana, T., Mizuno, H., Oshima, R., Takato, H., and Sugaya, T. (2021). Impact of loading topology and current mismatch on current–voltage curves of three-terminal tandem solar cells with interdigitated back contacts. Sol. Energy Mater. Sol. Cells *221*, 110901. https://doi.org/10.1016/j.solmat.2020.110901.

14. Adhyaksa, G.W.P., Johlin, E., and Garnett, E.C. (2017). Nanoscale Back Contact Perovskite Solar Cell Design for Improved Tandem Efficiency. Nano Lett. *17*, 5206–5212. https://doi.org/10.1021/acs.nanolett.7b01092.

15. Santbergen, R., Uzu, H., Yamamoto, K., and Zeman, M. (2019). Optimization of Three-Terminal Perovskite/Silicon Tandem Solar Cells. IEEE J. Photovolt. *9*, 446–451. https://doi.org/10.1109/JPHOTOV.2018.2888832.

16. Tockhorn, P., Wagner, P., Kegelmann, L., Stang, J.C., Mews, M., Albrecht, S., and Korte, L. (2020). Three-Terminal Perovskite/Silicon Tandem Solar Cells with Top and Interdigitated Rear Contacts. ACS Appl. Energy Mater. *3*, 1381–1392. https://doi.org/10.1021/acsaem.9b01800.

17. Park, I.J., Park, J.H., Ji, S.G., Park, M.A., Jang, J.H., and Kim, J.Y. (2019). A Three-Terminal Monolithic Perovskite/Si Tandem Solar Cell Characterization Platform. Joule *3*, 807–818. https://doi.org/10.1016/j.joule.2018.11.017.

18. Djebbour, Z., El-Huni, W., Dubois, A.M., and Kleider, J.P. (2019). Bandgap engineered smart three-terminal solar cell: New perspectives towards very high efficiencies in the silicon world. Prog. Photovolt. Res. Appl. *27*, 306–315. https://doi.org/10.1002/pip.3096.

19. Rienäcker, M., Warren, E.L., Wietler, T.F., Stradins, P., Tamboli, A.C., and Peibst, R. (2019). Three-Terminal Bipolar Junction Bottom Cell as Simple as PERC: Towards Lean Tandem Cell Processing. In Proceedings of the 46th IEEE Photovoltaic Specialists Conference (IEEE), pp. 2169–2175. https://doi.org/10.1109/PVSC40753.2019.8980645.

20. Warren, E.L., Deceglie, M.G., Rienäcker, M., Peibst, R., Tamboli, A., and Stradins, P. (2018). Maximizing tandem solar cell power extraction using a three-terminal design. Sustain. Energy Fuels *2*, 1141–1147. https://doi.org/10.1039/C8SE00133B.

21. Rienäcker, M., Warren, E.L., Schnabel, M., Schulte-Huxel, H., Niepelt, R., Brendel, R., Stradins, P., Tamboli, A., and Peibst, R. (2019). Back-contacted bottom cells with three terminals: Maximizing power extraction from current-mismatched tandem cells. Prog. Photovolt. Res. Appl. *27*, 410–423. https://doi.org/10.1002/pip.3107.

22. Gota, F., Langenhorst, M., Schmager, R., Lehr, J., and Paetzold, U.W. (2020). Energy Yield Advantages of Three-Terminal Perovskite-Silicon Tandem Photovoltaics. Joule *4*, 2387–2403. https://doi.org/10.1016/j.joule.2020.08.021.

23. Gee, J.M. (1988). A comparison of different module configurations for multi-band-gap solar cells. Solar Cells *24*, 147–155. https://doi.org/10.1016/0379-6787(88)90044-0.

24. Schulte-Huxel, H., Friedman, D., and Tamboli, A. (2018). String-Level Modeling of Two, Three, and Four Terminal Si-Based Tandem Modules. IEEE J. Photovolt. *8*, 1370–1375. https://doi.org/10.1109/JPHOTOV.2018.2855104.

25. McMahon, W.E., Schulte-Huxel, H., Buencuerpo, J., Geisz, J.F., Young, M.S., Klein, T.R., Tamboli, A.C., and Warren, E.L. (2021). Homogenous Voltage-Matched Strings using 3-Terminal Tandem Solar Cells: Fundamentals and End Losses. IEEE J. Photovolt. *11*, 1078. https://doi.org/10.1109/JPHOTOV.2021.3068325.

26. Witteck, R., Blankemeyer, S., Siebert, M., Kontges, M., and Schulte-Huxel, H. (2021). Partial shading of one solar cell in a photovoltaic module with 3-terminal cell interconnection. Sol. Energy Mater. Sol. Cells *219*, 110811. https://doi.org/10.1016/j.solmat.2020.110811.

27. Warren, E.L., McMahon, W.E., Rienäcker, M., VanSant, K.T., Whitehead, R.C., Peibst, R., and Tamboli, A.C. (2020). A Taxonomy for Three-Terminal Tandem Solar Cells. ACS Energy Lett. *5*, 1233–1242. https://doi.org/10.1021/acsenergylett.0c00068.

28. Geisz, J.F., France, R.M., Schulte, K.L., Steiner, M.A., Norman, A.G., Guthery, H.L., Young, M.R., Song, T., and Moriarty, T. (2020). Six-junction III–V solar cells with 47.1% conversion efficiency under 143 Suns concentration. Nat. Energy *5*, 326–335. https://doi.org/10.1038/s41560-020-0598-5.

29. Geisz, J.F., Buencuerpo, J., McMahon, W.E., Klein, T.R., Tamboli, A.C., and Warren, E.L. (2021). Fabrication, Measurement, and Modeling of GaInP/GaAs Three-Terminal Cells and Strings. In Proceedings of the 48th IEEE Photovoltiac Specialists Conference (IEEE), pp. 154–157. https://doi.org/10.1109/PVSC43889.2021.9518913.

30. Geisz, J.F., Kurtz, S., Wanlass, M.W., Ward, J.S., Duda, A., Friedman, D.J., Olson, J.M., McMahon, W.E., Moriarty, T., and Kiehl, J. (2007). High-efficiency GaInP/GaAs/InGaAs triple-junction solar cells grown inverted with a metamorphic bottom junction. Appl. Phys. Lett. *91*, 023502. https://doi.org/10.1063/1.2753729.

31. Green, M.A., Dunlop, E.D., Levi, D.H., Hohl-Ebinger, J., Yoshita, M., and Ho-Baillie, A.W.Y. (2019). Solar Cell Efficiency Tables (version 54). Prog. Photovolt. Res. Appl. *27*, 565–575. https://doi.org/10.1002/pip.3171.

32. Christians, J.A., Manser, J.S., and Kamat, P.V. (2015). Best Practices in Perovskite Solar Cell Efficiency Measurements. Avoiding the Error of Making Bad Cells Look Good. J. Phys. Chem. Lett. *6*, 852–857. https://doi.org/10.1021/acs.jpclett.5b00289.

33. Osterwald, C.R., Emery, K.A., Myers, D.R., and Hart, R.E. (1990). Primary reference cell calibrations, at SERI: History and methods. In Proceedings of the 21st IEEE Photovoltiac Specialists Conference (IEEE), pp. 1062–1067. https://doi.org/10.1109/PVSC.1990.111780.

34. Baur, C., Hermie, M., Dimroth, F., and Bett, A.W. (2007). Effects of optical coupling in III-V multilayer systems. Appl. Phys. Lett. *90*, 192109. https://doi.org/10.1063/1.2737927.

35. Steiner, M.A., Geisz, J.F., Moriarty, T.E., France, R.M., McMahon, W.E., Olson, J.M., Kurtz, S.R., and Friedman, D.J. (2013). Measuring IV Curves and Subcell Photocurrents in the Presence of Luminescent Coupling. IEEE J. Photovolt. *3*, 879–887. https://doi.org/10.1109/jphotov.2012.2228298.

36. Yoon, H., King, R.R., Kinsey, G., Kurtz, S., and Krut, D.D. (2003). Radiative Coupling Effects in GaInP/GaAs/Ge Multijunction Solar Cells. Proceedings of the 3rd World Conference on PV Energy Conversion, 745–748.

37. Steiner, M.A., and Geisz, J.F. (2012). Non-linear luminescent coupling in series-connected multijunction solar cells. Appl. Phys. Lett. *100*, 251106. https://doi.org/10.1063/1.4729827.

38. Tayagaki, T., Makita, K., Oshima, R., Mizuno, H., and Sugaya, T. (2018). Analysis of luminescence coupling effect in three-terminal tandem solar cells. J. Photonics Energy *8*, 045503. https://doi.org/10.1117/1.JPE.8.045503.

39. Essig, S., Steiner, M.A., Allebé, C., Geisz, J.F., Paviet-Salomon, B., Ward, J.S., Descoeudres, A., LaSalvia, V., Barraud, L., Badel, N., et al. (2016). Realization of GaInP/Si Dual-Junction Solar Cells With 29.8% 1-Sun Efficiency. IEEE J. Photovolt. *6*, 1012–1019. https://doi.org/10.1109/JPHOTOV.2016.2549746.

40. Steiner, M.A., Geisz, J.F., Ward, J.S., Garcia, I., Friedman, D.J., King, R.R., Chiu, P.T., France, R.M., Duda, A., Olavarria, W.J., et al. (2016). Optically enhanced photon recycling in mechanically stacked multijunction solar cells. IEEE J. Photovolt. *6*, 358–365. https://doi.org/10.1109/JPHOTOV.2015.2494690.

41. Geisz, J.F., Steiner, M.A., Garcia, I., France, R.M., McMahon, W.E., and Friedman, D.J. (2015). Generalized Optoelectronic model of series-connected multijunction solar cells. IEEE J. Photovolt. *5*, 1827–1839. https://doi.org/10.1109/JPHOTOV.2015.2478072.

42. Rau, U. (2007). Reciprocity relation between photovoltaic quantum efficiency and electroluminescent emission of solar cells. Phys. Rev. B *76*, 085303. https://doi.org/10.1103/Physrevb.76.085303.

43. King, R.R., Bhusari, D., Boca, A., Larrabee, D., Liu, X.Q., Hong, W., Fetzer, C.M., Law, D.C., and Karam, N.H. (2011). Band gap-voltage offset and energy production in next-generation multijunction solar cells. Prog. Photovolt. Res. Appl. *19*, 797–812. https://doi.org/10.1002/pip.1044.

44. Steiner, M.A., Geisz, J.F., Garcia, I., Friedman, D.J., Duda, A., and Kurtz, S.R. (2013). Optical enhancement of the open-circuit voltage in high quality GaAs solar cells. J. Appl. Phys. *113*, 123109. https://doi.org/10.1063/1.4798267.

45. Schnabel, M., Rienäcker, M., Warren, E.L., Geisz, J.F., Peibst, R., Stradins, P., and Tamboli, A.C. (2018). Equivalent perfomance in three-terminal and four-terminal tandem solar cells. IEEE J. Photovolt. *8*, 1584–1589. https://doi.org/10.1109/JPHOTOV.2018.2865175.

46. Bauer, A. (2012). ZnO:Al-Elektroden in semitransparenten organischen Solarzellen und Tandemsolarzellen (KIT Scientific Publishing).

47. Galiana, B., Algora, C., Rey-Stolle, I., and Garcia, I. (2005). A 3-D model for concentrator solar cells based on distributed circuit units. IEEE Trans. Electron Devices *52*, 2552–2558. https://doi.org/10.1109/TED.2005.859620.

48. Stradins, P., Rienäcker, M., Peibst, R., Tamboli, A., and Warren, E. (2019). A simple physical model for three-terminal tandem cell operation. In Proceedings of the 46th IEEE Photovoltaic Specialists Conference (IEEE), pp. 2176–2178. https://doi.org/10.1109/PVSC40753.2019.8980595.

49. Tayagaki, T., Makita, K., Tachibana, T., Mizuno, H., Oshima, R., Takato, H., and Sugaya, T. (2020). Three-Terminal Tandem Solar Cells With a Back-Contact-Type Bottom Cell Bonded Using Conductive Metal Nanoparticle Arrays. IEEE J. Photovolt. *10*, 358–362. https://doi.org/10.1109/JPHOTOV.2019.2957661.

50. Wilkins, M., Valdivia, C.E., Gabr, A.M., Masson, D., Fafard, S., and Hinzer, K. (2015). Luminescent coupling in planar opto-electronic devices. J. Appl. Phys. *118*, 143102. https://doi.org/10.1063/1.4932660.